

Electronic transport in helium-ion-beam etched encapsulated graphene nanoribbons

Nanda, Gaurav; Hlawacek, Gregor; Goswami, Srijit; Watanabe, Kenji; Taniguchi, Takashi; Alkemade, Paul F.A.

DOI

[10.1016/j.carbon.2017.04.062](https://doi.org/10.1016/j.carbon.2017.04.062)

Publication date

2017

Document Version

Final published version

Published in

Carbon

Citation (APA)

Nanda, G., Hlawacek, G., Goswami, S., Watanabe, K., Taniguchi, T., & Alkemade, P. F. A. (2017). Electronic transport in helium-ion-beam etched encapsulated graphene nanoribbons. *Carbon*, 119, 419-425. <https://doi.org/10.1016/j.carbon.2017.04.062>

Important note

To cite this publication, please use the final published version (if applicable). Please check the document version above.

Copyright

Other than for strictly personal use, it is not permitted to download, forward or distribute the text or part of it, without the consent of the author(s) and/or copyright holder(s), unless the work is under an open content license such as Creative Commons.

Takedown policy

Please contact us and provide details if you believe this document breaches copyrights. We will remove access to the work immediately and investigate your claim.



Electronic transport in helium-ion-beam etched encapsulated graphene nanoribbons



Gaurav Nanda^a, Gregor Hlawacek^b, Srijit Goswami^{a,d}, Kenji Watanabe^c, Takashi Taniguchi^c, Paul F.A. Alkemade^{a,*}

^a Kavli Institute of Nanoscience, Delft University of Technology, Lorentzweg 1, 2628 CJ, Delft, The Netherlands

^b Helmholtz-Zentrum Dresden-Rossendorf, Institut für Ionenstrahlphysik und Materialforschung, Bautzner Landstraße 400, D-01328, Dresden, Germany

^c National Institute for Materials Science, 1-1 Namiki, Tsukuba, 305-0044, Japan

^d QuTech, Delft University of Technology, Lorentzweg 1, 2628 CJ, Delft, The Netherlands

ARTICLE INFO

Article history:

Received 15 January 2017

Received in revised form

2 April 2017

Accepted 24 April 2017

Available online 27 April 2017

Keywords:

Helium ion microscope

Graphene

h-BN

Bandgap

Graphene nanoribbons

Electronic transport

ABSTRACT

We report the etching of and electronic transport in nanoribbons of graphene sandwiched between atomically flat hexagonal boron nitride (h-BN). The etching of ribbons of varying width was achieved with a focused beam of 30 keV He⁺ ions. Using in-situ electrical measurements, we established a critical dose of 7000 ions nm⁻² for creating a 10 nm wide insulating barrier between a nanoribbon and the rest of the encapsulated graphene. Subsequently, we measured the transport properties of the ion-beam etched graphene nanoribbons. Conductance measurements at 4 K show an energy gap, that increases with decreasing ribbon width. The narrowest ribbons show a weak dependence of the conductance on the Fermi energy. Furthermore, we observed power-law scaling in the measured current-voltage (*I*-*V*) curves, indicating that the conductance in the helium-ion-beam etched encapsulated graphene nanoribbons is governed by Coulomb blockade.

© 2017 The Authors. Published by Elsevier Ltd. This is an open access article under the CC BY-NC-ND license (<http://creativecommons.org/licenses/by-nc-nd/4.0/>).

1. Introduction

Graphene-based research has seen significant developments in the past decade, thanks to its unique band structure and extremely high mobilities [1,2]. Despite the high mobilities, graphene is a semi-metal without a bandgap which precludes applications in post-silicon electronics. Nevertheless, one can modify the electronic band structure by trimming graphene into nanoribbons. Under this geometrical constriction, quantum confinement and edge effects lead to a finite source-drain gap or a transport gap [3,4]. In their review paper, Bischoff et al. [4] noted that a stern distinction has to be made between a *source-drain gap* — i.e., the suppression of conductance in a limited source-drain voltage range — and a *transport gap* — i.e., the suppression in a limited gate voltage range. Also, it is known that the gap is greatly influenced by the presence of disorder in the graphene nanoribbons (GNRs) themselves [4,5]. Numerous techniques have been developed to create nanoribbons in graphene, such as plasma etching [4,6–9],

chemical synthesis [10–13], electron beam etching [14–16], and ion beam etching [17–21]. It is not straightforward, however, to make near-defect-free nanoribbons using the aforementioned techniques and, hence, it remains unclear how much the conductance and the presence of a gap are affected by edge effects, quantum confinement, and disorder [4].

Graphene devices are often fabricated on oxidized silicon substrates (SiO₂), which unfortunately lowers the mobility due to the presence of electron-hole puddles [22], charged impurity scattering [23], and contamination [18]. These adverse issues can be suppressed by encapsulating the graphene in hexagonal boron nitride (h-BN) [24]. As a consequence, the mobility in encapsulated graphene is typically an order of magnitude higher, comparable to that in suspended graphene [2,25,26]. In fact, Wang et al. [2] developed encapsulation with the specific purpose to safeguard graphene from effects caused by surface contaminations, such as PMMA residues introduced during device fabrication.

Because of its short de-Broglie wavelength, its sub-nanometer probe size, and the small beam spreading in materials [18,27,28], the focused ion beam (FIB) of a helium ion microscope (HIM) is an attractive tool for precise etching of encapsulated graphene devices. A recent experiment by Abbas et al. [21] with a He-FIB has

* Corresponding author.

E-mail address: P.F.A.Alkemade@tudelft.nl (P.F.A. Alkemade).

shown indications of bandgap opening in arrays of 5 nm wide graphene ribbons. Also, Nakaharai et al. [29] have shown, by conductance tuning, bandgap opening in narrow graphene channels, etched with a He⁺ beam. However, these measurements show very low conductance (~10,000 times higher resistivity than for pristine graphene), likely caused by the high number of beam defects and their pinning of surface contaminants. Since the paper by Kalhor et al. [30] it is known that exposure of graphene to helium ions leads to collateral damage in the non-exposed adjacent areas and to ion-beam-induced surface contamination [18]. A recent study by Nanda et al. [24] has shown that encapsulation of graphene in h-BN, with a ≤ 15 nm top h-BN layer, slows down the build-up of He⁺ beam damage in the exposed graphene and precludes detrimental effects due to beam-induced surface contamination. Moreover, this material shows *n*-doping and self-healing. However, fabrication of encapsulated graphene devices via focused He⁺ beam etching requires a good understanding of graphene's response to ion-beam bombardment and, thus, proper optimization of ion exposure doses. This understanding and process optimization are still wanting. For sure, a focused beam of 30 keV He⁺ ions can easily pass through several tens of nanometers of BN with limited loss of energy and without noticeable beam broadening [24,31]. If encapsulation influences ion-beam etching of graphene, the influence is direct and not via a change of the beam properties.

In this article we present transport properties of He⁺ beam etched encapsulated GNRs (graphene nanoribbons). The aim is to investigate the interaction between a focused helium ion beam and encapsulated graphene and the role of beam-induced damage in the conductance of graphene nanoribbons. The sub-nanometer He⁺ beam allows us to precisely control the size of the etched areas and in-situ electrical probes in the helium ion microscope enable us to determine quickly the minimal dose needed to isolate different parts of the graphene. The low-temperature measurements show an energy gap opening in narrow GNRs. We conclude that the gap arises due to the beam-induced disorder, leading to Coulomb blockade; the transport is governed by hopping between randomly distributed charged islands and localized states in the GNRs. We fabricated boron nitride/graphene/boron nitride sandwiches by stacking h-BN and graphene flakes via the van-der-Waals pick-up technique [24,32]. Ribbons were cut with a focused helium ion beam and devices were made by e-beam lithography, plasma etching, and Cr/Au deposition. Details of the entire procedure are reported in the supplementary data.

2. Experimental

2.1. Helium beam exposures and in-situ measurements

The fabrication procedure of the encapsulated graphene samples was similar to that of Nanda et al. [24]. We verified optically that the thickness of the top h-BN layer of all samples was 15 nm or less. Ion irradiation has been performed using a Carl Zeiss Orion NanoFab helium/neon ion microscope and the NPVE pattern generator from FIBICS Inc. The NanoFab is equipped with four MM3A-EM Kleindiek micro-manipulators for in-situ electrical probing. We used a 30 keV He⁺ beam at normal incidence and an ion current of 0.5 pA. The beam dwell time was 0.2 μ s and the beam step size 0.2 nm. The smallest aperture of 5 μ m was selected, giving the narrowest ion beam. The number of repeats was varied to achieve the desired dose (in steps of 1000 ions nm⁻²). Before each exposure, we took a low-resolution and low-dose image (≤ 0.5 ions nm⁻²) to locate the sample.

In-situ conductivity measurements in the ion microscope have been performed using two micro-manipulators with tungsten probes having tip radii below 100 nm. To minimize damage to the

BN/Gr/BN sandwich, the probes have been carefully brought into contact with the patterned gold leads. With a third probe placed onto the gold leads we checked that low resistance between the first two probes and the gold lead had been established. A source meter connected to the probes was used to measure the conductivity during ion irradiation.

2.2. Electrical and Raman spectroscopy measurements

Low-temperature direct current (DC) measurements were performed in a Leiden Cryogenics MCK-50 3He/4He dilution fridge. The DC currents and voltages were applied and probed with a home-built set-up. We carried out our low-temperature measurements at 4 K, although the set-up is able to reach a base temperature of 40 mK. Raman spectroscopy measurements were performed in air at room temperature with a Renishaw inVia Raman microscope. The spectrometer is equipped with a 514 nm laser with ~ 350 nm spot size. Sample heating is avoided by keeping the laser power below 1 mW.

3. Results and discussion

3.1. Device milling and characterization

Fig. 1a shows an optical image of the HIM chamber with micro-probes for the in-situ electrical measurements. The inset is a HIM micrograph of a number of devices with two probes in contact with one of them. The in-situ probes allow direct measurement of the relation between the ion dose and the electrical conductivity. Fig. 1b is a HIM micrograph of an array of encapsulated graphene devices, most of them 1 μ m \times 1 μ m in size. The devices were exposed to line doses ranging from 1000 to 10,000 ions nm⁻² with simultaneous monitoring of the resistance. All line cuts had a width of 10 nm. One example of a 1.2 μ m long and 10 nm wide cut is depicted in Fig. 1b and c as a white dotted line. The pristine devices had resistances between 5 and 10 k Ω , corresponding to resistivities between 5 and 10 k Ω/\square . Several independent measurement series were conducted on different samples and we observed good reproducibility in the resistance.

The resistance vs. ion dose is plotted in Fig. 1c. One sees that the resistance increased almost exponentially up to a critical dose of 7000 ions nm⁻², where the circuit became open. In this regard, the in-situ measurements provide a unique knob to monitor the endpoint detection and dose determination of the encapsulated graphene devices. Although this critical dose is specific for our experimental conditions, we expect that scaling via the nuclear energy loss, ion-target mass ratios, and binding energies can be used to estimate the critical dose for other ion species and energies and other encapsulated 2D materials. Subsequently, we used this critical dose to etch nanoribbons in encapsulated graphene of 200 nm in length and with widths of 90, 70, 50, 35, 25, and 10 nm. Fig. 2a–c shows helium ion micrographs of various GNRs. Fig. 2d shows a device (Dev1), also shown in Fig. 1b, where a dose of 7000 ions nm⁻² is applied to make a 35 nm wide ribbon. The two side contacts (SC1 and SC2) are used to check that there is no residual conductivity between the isolated regions. The inset shows that indeed no measurable current flowed between SC1 and SC2; the resistance is > 1 G Ω . Fig. 2e shows an AFM image of three 10 nm line exposures with 7000 ions nm⁻². The full-width-at-half-maximum (FWHM) of the etched line is 10 nm, see the AFM profile. Note that the widths of the etch line in the HIM image (Fig. 2b) and in the AFM profile are both equal to the designed line width of 10 nm.

We performed Raman mapping around the etched line to investigate the lateral damage in the exposed graphene. Ion-induced defects in single-layer graphene can be studied via the

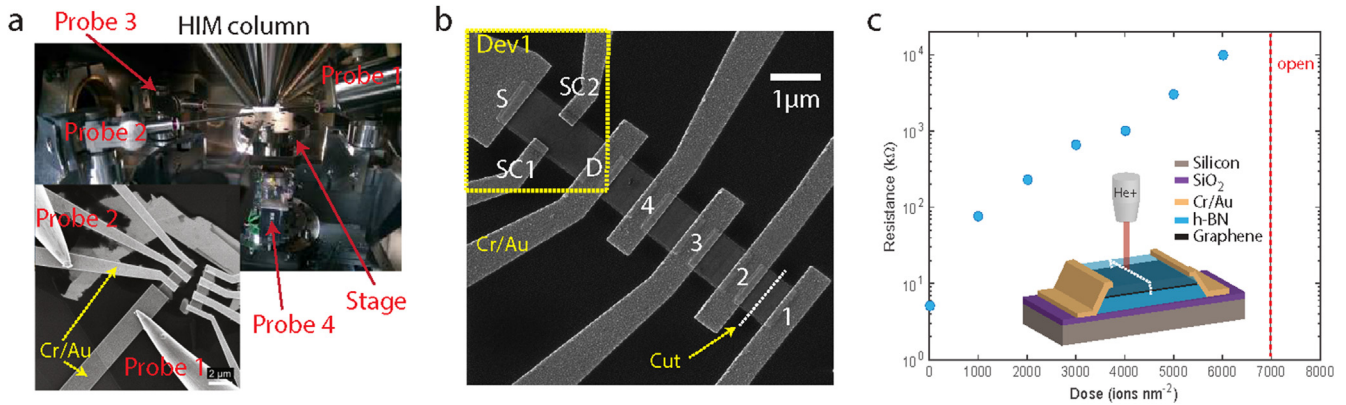


Fig. 1. (a) Optical image of four micro-manipulators used to electrically probe the sample in the helium ion microscope (HIM) chamber. The inset shows a helium ion micrograph of the probes contacting the Cr/Au leads of the sample. (b) He^+ micrograph of multiple graphene devices fabricated in a h-BN/graphene/h-BN sandwich, stacked via the van-der-Waals pick-up technique. The probes are applied to pairs of contacts (e.g. 1–2 or 2–3), and the resistance between them is measured by applying a voltage across the contacts. (c) In-situ dose optimization in the HIM. The resistance between the two leads increases as a function of dose until an open circuit is reached at $7000 \text{ ions nm}^{-2}$. The inset depicts the device during line cutting. (A colour version of this figure can be viewed online.)

evolution of the D-peak in the Raman spectrum [33–35]. The Raman map of the D-peak is shown in Fig. 2f. Because of the narrow and localized interaction volume of the He^+ beam in the outermost few dozens of nanometers [24,31,36], most of the ion beam damage is expected to be concentrated in the 10 nm etched lines. Yet, the measured D-peak intensity decays up to $\sim 200 \text{ nm}$ on both sides of the exposure area. This result is, however, limited by the relatively large laser spot size ($\sim 350 \text{ nm}$) of our Raman spectrometer. Fig. 2g shows Raman spectra before and after etching. Before etching, the signature of single-layer graphene is clearly discernible; in particular the 2D peak intensity is ~ 4 times higher than that of the G

peak and a D peak is absent, both are signs of high-quality graphene. After etching, a small but significant D-peak is visible as a shoulder on the h-BN peak at 1345 cm^{-1} , thus indicating atomic disorder [24,34]. The 2D peak is still visible, which indicates that the crystalline structure of graphene is still partly intact within the probe size ($\sim 350 \text{ nm}$) of the Raman beam [24,37].

3.2. Low-temperature transport in GNRs

To characterize the electronic properties of the GNRs, transport measurements were conducted. The room temperature current-

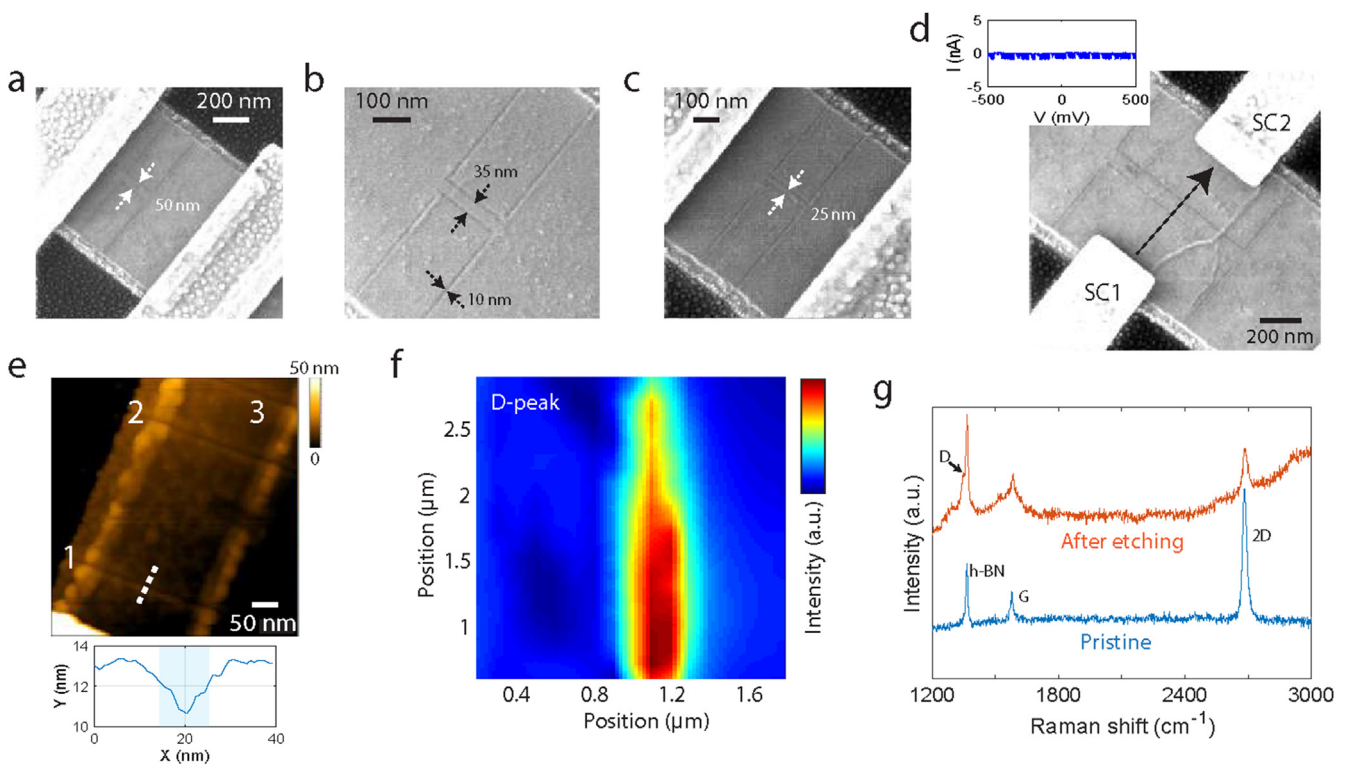


Fig. 2. (a–c) Helium ion micrographs of nanoribbons with widths of 50, 35, and 25 nm, respectively. (d) Blow-up of the yellow box in Fig. 1b. A source-drain bias is applied between side contact 1 (SC1) and side contact 2 (SC2). The inset shows the measured source-drain current. A 10 nm wide line cut with a dose of $7000 \text{ helium ions nm}^{-2}$ is sufficient to create an insulating barrier. (e) AFM images of three 10 nm line exposures with $7000 \text{ ions nm}^{-2}$. The lower figure shows the line profile across cut 1. (f) D-peak Raman map of the 10 nm line cut region. (g) Raman spectra of the pristine sample and of the 25 nm wide etched nanoribbon device. (A colour version of this figure can be viewed online.)

voltage (I - V) characteristics in Fig. 3a show a linear behaviour in the 35 and 50 nm wide ribbons and a slight non-linearity in the 25 nm ribbon. The room temperature resistivity of the 50 nm wide ribbon is $\sim 50 \text{ k}\Omega/\square$. The inset shows the conductance ($1/R$) of the 10–50 nm wide ribbons, all made from the same stack, as a function of the ribbon width. Except for the smallest ribbon, the conductance increases more or less linearly with the width, suggesting a $\sim 8 \text{ nm}$ inactive layer at both edges of the ribbons. As we cool the samples to 4 K, non-linearity clearly appears, see Fig. 3b for the 35 nm ribbon. The non-linearity in the I - V characteristics depends on the ribbon width, see Fig. 3c. Fig. 3d shows the differential conductance (dI/dV) of the 35 nm wide ribbon at 4 K as a function of the bias voltage V_{SD} ; approaching zero in the $\sim 100 \text{ mV}$ range around zero bias voltage. The appearance of non-linear I - V characteristics is an indication of an energy gap (E_{gap}) in the GNRs [15,38]. Non-linear I - V characteristics have recently been reported for He^+ beam etched ribbons in supported graphene [29] and for electron beam etched ribbons in suspended graphene [15,16].

Fig. 4 shows DC-conductance measurements at 4 K. We studied the influence of the voltage applied to the bottom gate (V_{BG}) on the

source-drain current (I_{SD}). Note that the I_{SD} of the narrowest ribbons is low because of their high resistance; therefore we applied a higher V_{SD} bias for the 25 and 35 nm ribbons. One can clearly see that the position of the minimum current shifts to more negative V_{BG} with decreasing width, thus indicating a higher electron doping level in the narrower ribbons. This effect is due to beam induced n -doping of graphene, likely by collision-induced C-N exchange [24]. Apparently, the strong n -doping of the 25 nm ribbon is due to the close proximity of the central region of the ribbon to the heavily damaged regions near its edges.

From the DC-conductance as a function of gate bias (V_{BG}) and source-drain bias (V_{SD}), one can estimate the energy of the source-drain gap [6–8]. Previous bias spectroscopy measurements in narrow ribbons have shown the formation of overlapping Coulomb diamonds, signifying suppression in conductance by Coulomb blockade [4,6–8]. The Coulomb blockade is caused by the interaction between charge carriers and localized charges, e.g. of islands, impurities or defects [4]. Therefore, the energy gap is related to the voltage of the largest diamond (V_{SD}^*) as $E_{gap} = eV_{SD}^*$ [6–8] (see the arrow in Fig. 4b). The 90 nm ribbon shows a small source-drain gap

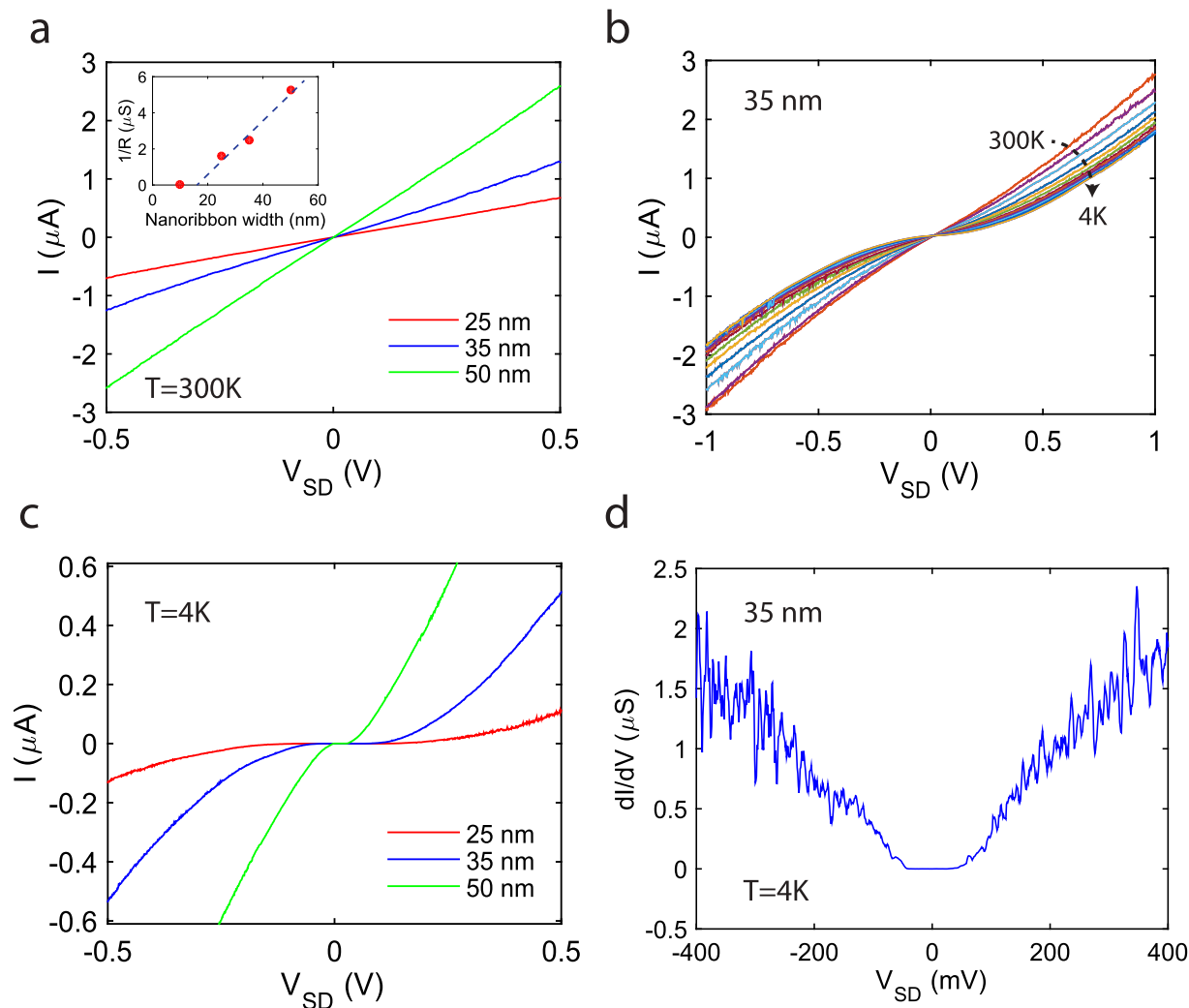


Fig. 3. (a) Source-drain bias (V_{SD}) dependence of the drain current (I_{SD}) at room temperature in the nanoribbons. The inset shows the relation between nanoribbon width and the conductance ($1/R$). (b) V_{SD} dependence of the I_{SD} for the 35 nm ribbon as a function of temperature. (c) V_{SD} dependence of the I_{SD} for the 25, 35, and 50 nm ribbons at 4 K. (d) Differential conductance (dI/dV) as a function of V_{SD} for the 35 nm ribbon, showing zero conductance near zero source-drain bias. The back gate bias (V_{BG}) for all figures is zero. (A colour version of this figure can be viewed online.)

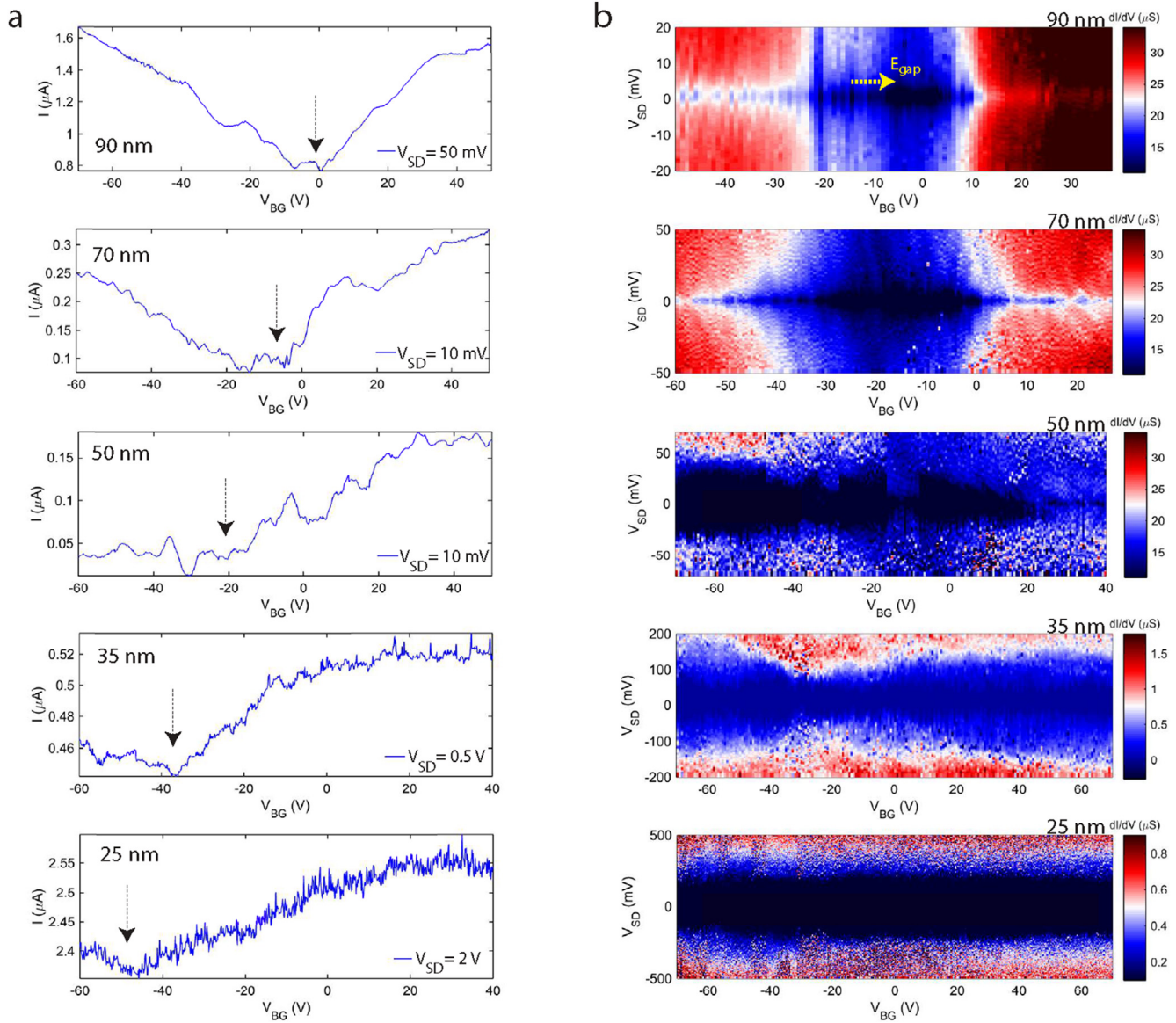


Fig. 4. (a) Back-gate bias (V_{BG}) dependence of the drain current (I_{SD}) for fixed source-drain bias (V_{SD}). The onsets of the charge neutrality point are marked with arrows. (b) Colour plots of the source-drain current (I_{SD}) as a function of V_{BG} and V_{SD} for nanoribbons with a length of 200 nm and a width of 25, 35, 50, 70, and 90 nm. The yellow arrow in the plot of the 90 nm ribbon refers to the V_{SD} of the largest diamond. It determines the energy gap ($= eV_{SD}$). All measurements were taken at 4 K. (A colour version of this figure can be viewed online.)

(< 5 meV) which is gate dependent. As the width of the ribbon decreases, E_{gap} increases, reaching a maximum of 180 meV in the 25 nm wide ribbon. Also, one can notice that the gate response of the 25 nm ribbon is very weak. The E_{gap} in our 25 nm ribbon is larger than the gap reported by Han et al. [6] for 25 nm ribbons made by plasma etching, in fact, it is close to the value for their 15 nm ribbons. This discrepancy could be due to extra beam-induced damage near the edges of our GNRs. As mentioned before, there is an inactive strip of ~ 8 nm wide at the edges of the ribbons, see the inset of Fig. 3a.

In contrast, Evaldsson *et al.* [3] inferred that not Coulomb blockade but Anderson-type localization, induced by edge disorder, is responsible for the energy gap in plasma-etched GNRs. Naitou et al. [39] have observed a metal-insulator transition in supported graphene for a He^+ beam dose of 120 ions nm^{-2} . They also related this transition to Anderson-type localization caused by beam-induced disorder; they estimated the localization length to lie between 20 and 50 nm. The beam-induced disorder near the edges of

our ribbons was very high and, therefore, we expect a finite region in the GNR to be non-conducting (discussed later in Fig. 5). Indeed, our 10 nm wide ribbons did not show any conductance and the other ribbons had an inactive region of ~ 8 nm at each edge. This value is in reasonably good agreement with the disorder radius of at least 10 nm, *i.e.* half the minimal localization length, found by Naitou et al. [39]. Moreover, it is only slightly larger than that of the GNRs of Han et al. [6]: 7 nm at each edge in conductance measurements at 1.7 K.

3.3. Model for defect-induced transport in GNRs

The disorder arising from beam-induced defects breaks the ideal two-dimensional (2-D) lattice of graphene down into isolated islands, causing inhomogeneities in the charge distribution and in conductance when voltages are applied [40]. A sketch illustrating the presumed damage extent in our graphene exposed to the etching He^+ beam is shown in Fig. 5a. In general, focused ion beams

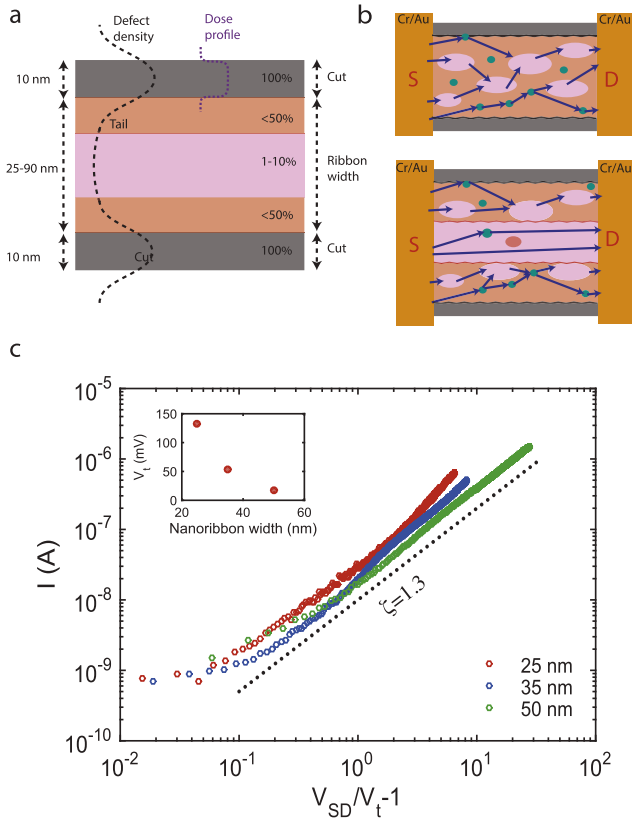


Fig. 5. (a) Sketch showing the defect density in graphene, built-up during etching with a focused He^+ beam. The assumed defect density decays within a few nanometers outside the actual 10 nm wide etch cut. The centre of the ribbon between the two cuts has a low but finite defect density caused by beam tails, by beam broadening in the material, and by defect diffusion. In reality, the boundaries between the various regions are rough. (b) Sketch illustrating a few possible paths of carrier transport in a narrow (upper) and a wide (lower) GNR; in contrast to 5a, the roughness of the boundaries is taken into account. The pink regions represent relatively intact graphene (either charged islands or a continuous strip) and the green circles are defect sites. The dark blue solid arrows depict examples of carrier transport through charged islands and defect sites. (c) Measured current as a function of $V_{SD}/V_t - 1$ on a log-log plot showing power-law scaling (same data as in Fig. 3c). The dotted line is a curve with $\zeta = 1.3$. The inset shows the variation of the threshold voltage (V_t) with nanoribbon width. (A colour version of this figure can be viewed online.)

have a Gaussian shape with finite tails [41]. For our He^+ beam, unfortunately, of unknown width and intensity. We assume that the lateral extent of the damage in our encapsulated graphene is determined by ions from the beam tail, by beam broadening in the top h-BN layer, by defect diffusion, and by edge modification via C-N exchange. Also backscattered ions and recoiled atoms can cause damage in the graphene outside the exposure areas. Recoiled atoms, however, do not travel far and have little energy, whereas backscattered helium ions in low-Z materials such as BN are rare and dispersed over a wide area. The He^+ beam broadening in h-BN encapsulated graphene has been studied previously by Nanda et al. [24] using SRIM simulations: it is less than 1 nm in 15 nm h-BN. The extent of the other mechanisms is largely unknown, but obviously they are relatively more severe for the smaller ribbons. Fig. 5b shows a sketch of islands and defect sites in a narrow (upper) and a wide GNR (lower), inspired by a similar figure in Ref. [42]. The transport through the narrow GNR is predominantly governed by charge hopping between the islands and the defects, showing up as Coulomb blockade. The wide GNRs have also a central region with a low defect density, allowing charge carriers to reach the drain electrode with or without scattering.

For our smaller GNRs (25 and 35 nm), diamonds of suppressed conductance overlap (see Fig. 4b), similarly as described by Gallagher *et al.* for quantum dots in GNRs [8]. To provide more evidence of the presence of localized states in our GNRs, we analyzed the I - V characteristics using the model of Middleton and Wingreen (MW) [43], who have studied the transport in arrays of metallic dots. In their work, the current I scales as:

$$I \sim \left[\frac{V_{SD}}{V_t} - 1 \right]^\zeta, \quad (1)$$

where ζ is a power-law exponent and V_t is the threshold voltage below which the current is virtually absent. Above V_t , the applied source-drain bias is large enough to populate the islands with electrons or holes, causing the current to flow through the entire nanoribbon. Previous experiments have shown this scaling behaviour in arrays of metallic islands [44], in graphene quantum dot arrays [40], in disordered MoS_2 nanoflakes [42], and in a quantum dot lattice in GaAs [45]. Fig. 5c shows the measured current in our narrower ribbons on a log-log scale, obeying indeed the scaling law of Equation (1). The curves for different ribbon widths have different values of V_t . Nevertheless, they exhibit a reasonably clear collapse into a single trace with $\zeta = 1.3 \pm 0.1$. For the 70 and 90 nm ribbons $\zeta \approx 1.2$ (see supplementary data). The larger values for V_t of the narrower ribbons indicate that the islands in these ribbons are relatively small. According to the MW model, the characteristic exponent ζ is determined by the dimensionality of the conducting channels. For a 1-D system, with only one dominant path or with a small number of preferred paths, ζ equals 1, whereas for a 2-D system it is between 1.6 and 2 [42,43]. Since ζ is always ~ 1.3 in our nanoribbons, we conclude that the transport in all ribbons is mediated by multiple hops of the charge carriers between localized states and islands, mainly dispersed along the ribbon length. Contrary to intuition, we do not see in the hopping conductance a gradual transition from a 1-D character in the narrowest ribbons (~ 30 nm) to a more 2-D character in the wider ones (~ 80 nm). The corresponding transport mechanism in our ribbons is sketched in Fig. 5b.

4. Conclusions

We have demonstrated the successful fabrication of nanoribbon devices in h-BN encapsulated graphene via etching with a focused He^+ beam. We have measured the conductance of graphene nanoribbons (GNRs) with widths between 25 and 90 nm. At room temperature and without gate bias, the resistivity of the wider ribbons (> 50 nm) was typically ~ 50 k Ω/\square , about 5–10 times higher than that of the pristine graphene. The bias spectroscopy measurements of the wider ribbons show Coulomb diamonds in a limited gate-voltage range. However, for the narrow ribbons, Coulomb diamonds had merged and formed a broad band with an almost constant energy gap, independent of the Fermi energy. At 4 K, we found an energy gap (E_{gap}) of 180 meV for the 25 nm wide ribbon. The narrower ribbons exhibited higher resistivities and a higher E_{gap} , likely due to the influence of ~ 8 nm wide inactive strips at their edges. Unfortunately, our Raman spectrometer cannot resolve the disorder radius; for that purpose tip-enhanced Raman spectroscopy (TERS) would be needed. The I - V characteristics of the GNRs follow power-law scaling with an exponent ζ of 1.3 ± 0.1 , confirming that Coulomb blockade determines the charge transport [40,43,44]. In our understanding, the quantum dots, responsible for the Coulomb blockade, are generated by beam-induced disorder. It would be very interesting to measure the beam-induced exchange of atoms between the graphene and the

encapsulating BN material, for instance by local optical techniques that probe C–N or C–B bonds.

In conclusion, the transport in our FIB-etched encapsulated GNRs is best described in terms of a series of overlapping quantum dots, in which the current suppression is due to Coulomb blockade. We attribute the almost complete disappearance of conductance in previous studies on unprotected graphene [17–21,29,30] to contamination that is aggravated by beam-induced disorder. Finally, we note that the in-situ current probes in the helium ion microscope are very useful for efficient dose optimization and end-point detection during focused ion beam etching. We expect that the findings of this study are crucial for focused ion beam nano-patterning of 2-D materials for the realization of e.g. electronic and spintronic nanodevices.

Acknowledgements

The authors thank the Dutch Technology Foundation STW, which is part of The Netherlands Organization for Scientific Research (NWO), and the Ministry of Economic Affairs for funding this research (STW project number 12205). The growth of hexagonal boron nitride crystals was supported by the Elemental Strategy Initiative conducted by the MEXT, Japan and JSPS KAKENHI (grant numbers JP26248061, JP15K21722 and JP25106006).

Appendix A. Supplementary data

Supplementary data related to this article can be found at <http://dx.doi.org/10.1016/j.carbon.2017.04.062>.

References

- [1] K.S. Novoselov, A.K. Geim, S.V. Morozov, D. Jiang, M.I. Katsnelson, I.V. Grigorieva, S.V. Dubonos, A.A. Firsov, Two-dimensional gas of massless dirac fermions in graphene, *Nature* 438 (2005) 197–200.
- [2] L. Wang, I. Meric, P.Y. Huang, Q. Gao, Y. Gao, H. Tran, T. Taniguchi, K. Watanabe, L.M. Campos, D.A. Muller, J. Guo, P. Kim, J. Hone, K.L. Shepard, C.R. Dean, One-dimensional electrical contact to a two-dimensional material, *Science* 342 (2013) 614–617.
- [3] M. Ewaldsson, I.V. Zozoulenko, H. Xu, T. Heinzel, Edge-disorder-induced anderson localization and conduction gap in graphene nanoribbons, *Phys. Rev. B* 78 (2008) 161407.
- [4] D. Bischoff, A. Varlet, P. Simonet, M. Eich, H.C. Overweg, T. Ihn, K. Ensslin, Localized charge carriers in graphene nanodevices, *Appl. Phys. Rev.* 2 (031301) (2015).
- [5] F. Molitor, A. Jacobsen, C. Stampfer, J. Güttinger, T. Ihn, K. Ensslin, Transport gap in side-gated graphene constrictions, *Phys. Rev. B* 79 (075426) (2009).
- [6] M.Y. Han, B. Özyilmaz, Y. Zhang, P. Kim, Energy band-gap engineering of graphene nanoribbons, *Phys. Rev. Lett.* 98 (2007) 206805.
- [7] C. Stampfer, J. Güttinger, S. Hellmüller, F. Molitor, K. Ensslin, T. Ihn, Energy gaps in etched graphene nanoribbons, *Phys. Rev. Lett.* 102 (056403) (2009).
- [8] P. Gallagher, K. Todd, D. Goldhaber-Gordon, Disorder-induced gap behavior in graphene nanoribbons, *Phys. Rev. B* 81 (2010) 115409.
- [9] Y. Lu, B. Goldsmith, D.R. Strachan, J.H. Lim, Z. Luo, A.T. Charlie Johnson, High-on/off-ratio graphene nanoconstriction field-effect transistor, *Small* 6 (2010) 2748–2754.
- [10] X. Li, Xinran Wang, L. Zhang, S. Lee, H. Dai, Chemically derived, ultrasmooth graphene nanoribbon semiconductors, *Science* 319 (2008) 1229.
- [11] T. Shimizu, J. Haruyama, D.C. Marcano, D.V. Kosinkin, J.M. Tour, K. Hirose, K. Suenaga, Large intrinsic energy bandgaps in annealed nanotube-derived graphene nanoribbons, *Nat. Nanotechnol.* 6 (2011) 45–50.
- [12] D.V. Kosynkin, A.L. Higginbotham, A. Sinitskii, J.R. Lomeda, A. Dimiev, B.K. Price, J.M. Tour, Longitudinal unzipping of carbon nanotubes to form graphene nanoribbons, *Nature* 458 (2009) 872–876.
- [13] W. Yoon, Y. Lee, H. Jang, M. Jang, J.S. Kim, H.S. Lee, S. Im, D.W. Booa, J. Park, S.-Y. Ju, Graphene nanoribbons formed by a sonochemical graphene unzipping using flavin mononucleotide as a template, *Carbon* 81 (2015) 629–638.
- [14] B. Sommer, J. Sonntag, A. Ganczarczyk, D. Braam, G. Prinz, A. Lorke, M. Geller, Electron-beam induced nano-etching of suspended graphene, *Sci. Rep.* 5 (2015) 7781.
- [15] Q. Wang, R. Kitaura, S. Suzuki, Y. Miyauchi, K. Matsuda, Y. Yamamoto, S. Arai, H. Shinohara, Fabrication and in situ transmission electron microscope characterization of free-standing graphene nanoribbon devices, *ACS Nano* 10 (2016) 1475–1480.
- [16] J.A. Rodriguez-Manzo, Z.J. Qi, A. Crook, J.H. Ahn, A.T.C. Johnson, M. Drndić, In situ transmission electron microscopy modulation of transport in graphene nanoribbons, *ACS Nano* 10 (2016) 4004–4010.
- [17] D. Pickard, L. Scipioni, Graphene Nano-ribbon Patterning in the Orion Plus, Zeiss Application Note, 2009.
- [18] M.C. Lemme, D.C. Bell, J.R. Williams, L.A. Stern, B.W.H. Baugher, P. Jarillo-Herrero, C.M. Marcus, Etching of graphene devices with a helium ion beam, *ACS Nano* 3 (2009) 2674–2676.
- [19] Y. Zhang, C. Hui, R. Sun, K. Li, K. He, X. Ma, F. Liu, A large-area 15 nm graphene nanoribbon array patterned by a focused ion beam, *Nanotechnology* 25 (2014) 135301.
- [20] D.C. Bell, M.C. Lemme, L.A. Stern, J.R. Williams, C.M. Marcus, Precision cutting and patterning of graphene with helium ions, *Nanotechnology* 20 (2009) 455301.
- [21] A.N. Abbas, G. Liu, B. Liu, L. Zhang, H. Liu, D. Ohlberg, W. Wu, C. Zhou, Patterning, characterization, and chemical sensing applications of graphene nanoribbon arrays down to 5 nm using helium ion beam lithography, *ACS Nano* 8 (2014) 15381546.
- [22] J. Martin, N. Akerman, G. Ulbricht, T. Lohmann, J.H. Smet, K. von Klitzing, A. Yacoby, Observation of electronhole puddles in graphene using a scanning single-electron transistor, *Nat. Phys.* 4 (2008) 144–148.
- [23] J.H. Chen, C. Jang, S. Adam, M.S. Fuhrer, E.D. Williams, M. Ishigami, Charged-impurity scattering in graphene, *Nat. Phys.* 4 (2008) 377–381.
- [24] G. Nanda, S. Goswami, K. Watanabe, T. Taniguchi, P.F.A. Alkemade, Defect control and n-doping of encapsulated graphene by helium-ion-beam irradiation, *Nano Lett.* 15 (2015) 4006–4012.
- [25] X. Du, I. Skachko, A. Barker, E.Y. Andrei, Approaching ballistic transport in suspended graphene, *Nat. Nanotechnol.* 3 (2008) 491–495.
- [26] C.R. Dean, A.F. Young, I. Meric, C. Lee, L. Wang, S. Sorgenfrei, K. Watanabe, T. Taniguchi, P. Kim, K.L. Shepard, J. Hone, Boron nitride substrates for high quality graphene electronics, *Nat. Nanotechnol.* 5 (2010) 722–726.
- [27] M. Ananth, L. Stern, D. Ferranti, C. Huynh, J. Notte, L. Scipioni, C. Sanford, B. Thompson, Creating nanohole arrays with the helium ion microscope, *Proc. SPIE* 8036 (2011) 8036M.
- [28] G. Hlawacek, V. Veligura, R. van Gastel, B. Poelsema, Helium ion microscopy, *J. Vac. Sci. Technol. B* 32 (020801) (2014).
- [29] S. Nakaharai, T. Iijima, S. Ogawa, S. Suzuki, S.L. Li, K. Tsukagoshi, S. Sato, N. Yokoyama, Conduction tuning of graphene based on defect-induced localization, *ACS Nano* 7 (2013) 5694–5700.
- [30] N. Kalthor, S.A. Boden, H. Mizuta, Sub-10 nm patterning by focused he-ion beam milling for fabrication of downscaled graphene nano devices, *Microelectron. Eng.* 114 (2014) 70–77.
- [31] D. Cohen-Tanugi, N. Yao, Superior imaging resolution in scanning helium-ion microscopy: a look at beam-sample interactions, *J. Appl. Phys.* 104 (063504) (2008).
- [32] Victor E Calado, Srijit Goswami, G. Nanda, M. Diez, A.R. Akhmerov, K. Watanabe, T.M. Klapwijk, T. Taniguchi, L.M.K. Vandersypen, Ballistic josephson junctions in edge-contacted graphene, *Nat. Nanotechnol.* 10 (2015) 761–764.
- [33] A.C. Ferrari, J.C. Meyer, V. Scardaci, C. Casiraghi, M. Lazzeri, F. Mauri, S. Piscanec, D. Jiang, K.S. Novoselov, S. Roth, A.K. Geim, Raman spectrum of graphene and graphene layers, *Phys. Rev. Lett.* 97 (2006) 187401.
- [34] A.C. Ferrari, Raman spectroscopy of graphene and graphite: disorder, electron-phonon coupling, doping and nonadiabatic effects, *Solid State Commun.* 143 (2007) 47–57.
- [35] A.C. Ferrari, D.M. Basko, Raman spectroscopy as a versatile tool for studying the properties of graphene, *Nat. Nanotechnol.* 8 (2013) 235–246.
- [36] J. Buchheim, R.M. Wyss, I. Shorubalko, H.G. Park, Understanding the interaction between energetic ions and freestanding graphene towards practical 2d perforation, *Nanoscale* 8 (2016) 8345–8354.
- [37] L.G. Cancado, A. Jorio, E.H.M. Ferreira, F. Stavale, C.A. Achete, R.B. Capaz, M.V.O. Moutinho, A. Lombardo, T.S. Kulmala, A.C. Ferrari, Quantifying defects in graphene via raman spectroscopy at different excitation energies, *Nano Lett.* 11 (2011) 3190–3196.
- [38] M.W. Lin, C. Ling, L.A. Agapito, N. Kioussis, Y. Zhang, M.M.C. Cheng, W.L. Wang, E. Kaxiras, Z. Zhou, Approaching the intrinsic band gap in suspended high-mobility graphene nanoribbons, *Phys. Rev. B* 84 (2011) 125411.
- [39] Y. Naitou, S. Ogawa, Anderson localization of graphene by helium ion irradiation, *Appl. Phys. Lett.* 108 (2016) 171605.
- [40] D. Joung, L. Zhai, S.I. Khondaker, Coulomb blockade and hopping conduction in graphene quantum dots array, *Phys. Rev. B* 83 (2011) 115323.
- [41] R.L. Kubena, J.W. Ward, Current density profiles for a ga^+ ion microprobe and their lithographic implications, *Appl. Phys. Lett.* 51 (1960) 1987.
- [42] S.T. Lo, O. Klochan, C.H. Liu, W.H. Wang, A.R. Hamilton, C.T. Liang, Transport in disordered monolayer mos_2 nanoflakes evidence for inhomogeneous charge transport, *Nanotechnology* 25 (2014) 375201.
- [43] A.A. Middleton, N.S. Wingreen, Collective transport in arrays of small metallic dots, *Phys. Rev. Lett.* 71 (1993) 3198.
- [44] A.J. Rimberg, T.R. Ho, J. Clarke, Scaling behavior in the current-voltage characteristic of one- and two-dimensional arrays of small metallic islands, *Phys. Rev. Lett.* 74 (1995) 4714.
- [45] S. Goswami, M.A. Aamir, C. Siegert, M. Pepper, I. Farrer, D.A. Ritchie, A. Ghosh, Transport through an electrostatically defined quantum dot lattice in a two-dimensional electron gas, *Phys. Rev. B* 86 (2012) 119904.